

## Research Article

# Protective Ceramic Coatings for Solid Oxide Fuel Cell (SOFC) Balance-of-Plant Components

Raymond L. Winter,<sup>1</sup> Prabhakar Singh,<sup>2</sup> Mark K. King Jr.,<sup>3</sup> Manoj K. Mahapatra,<sup>3</sup> and Uma Sampathkumaran <sup>1</sup>

<sup>1</sup>InnoSense LLC, Torrance 90505, USA

<sup>2</sup>Department of Materials Science & Engineering, University of Connecticut, Storrs, CT, USA

<sup>3</sup>Department of Materials Science and Engineering, University of Alabama at Birmingham, Birmingham, Alabama 35294, USA

Correspondence should be addressed to Uma Sampathkumaran; [uma.sampathkumaran@innosensellc.com](mailto:uma.sampathkumaran@innosensellc.com)

Received 31 May 2018; Revised 6 August 2018; Accepted 19 August 2018; Published 14 October 2018

Academic Editor: Meilin Liu

Copyright © 2018 Raymond L. Winter et al. This is an open access article distributed under the Creative Commons Attribution License, which permits unrestricted use, distribution, and reproduction in any medium, provided the original work is properly cited.

Solid oxide fuel cells (SOFCs) have the potential to meet the growing need for electrical power generation if the cost per megawatt can be further reduced. Currently, SOFC stacks are replaced too frequently to be cost competitive. SOFC service life can be extended by preventing chromium- (Cr-) bearing species from evaporating from the interior surfaces of balance of plant (BOP) components and poisoning the cathode to increase the lifetime. We have developed yttria-stabilized zirconia (YSZ) and aluminum oxide- ( $\text{Al}_2\text{O}_3$ -) modified sol-gel paints or inks for coating BOP components. 430 stainless steel (430SS) substrates with three surface conditions were coated with the 0.8–1.5  $\mu\text{m}$  thick YSZ and  $\text{Al}_2\text{O}_3$  paints. The coated 430SS samples were tested for thermal cycling resistance, thermal soak, and Cr evaporation. Thermal soak and thermal cycling test results show promise for the YSZ-coated 430SS substrates. The Cr evaporation test of a coated substrate showed a 51% reduction in Cr generation, when compared with a bare substrate.

## 1. Introduction

Fossil fuel-based power generation systems are the mainstay of electrical power production in many countries today. These systems, however, contribute to increase in airborne pollutants carbon dioxide ( $\text{CO}_2$ ) emission level leading to potential climate change and global warming. Generally, peak electrical power is met by small- and medium-sized present gas-fired electrical power plants. These plants produce 85% of the air pollution generated by electrical power generation in the USA, along with relatively low fuel consumption efficiency. One of the Department of Energy's (DOE's) goals is to integrate solid oxide fuel cell (SOFC) technologies as an alternative for clean energy systems that can feed into the nation's power grid. Currently, one of the constraints limiting the operational life of a SOFC plant is the poisoning of electrodes from the chromium- (Cr-) bearing volatile materials from stainless steel balance of plant (BOP) components. Various chemical

reactions can take place at a lanthanum strontium manganite (LSM) cathode, due to Cr poisoning. In all cases, the integrity of the LSM is compromised. The result is a change in the chemistry and therefore the electrochemistry of the cathode, rendering it incapable of performing its proper electrochemical function in the SOFC. The extended power plant life is key to making power grid SOFCs a cost-effective reality. The target is a 10-year service life.

Even though perovskite coatings like LSC ( $\text{LaScCrO}_3$ ), LSM ( $\text{LaSrMnO}_3$ ), and LSCF ( $\text{LaSrCoFeO}_3$ ) decrease Cr evaporation [1, 2], they suffer from spallation and difficulty in adhesion of the coatings [3]. Spinel coatings based on cobalt and its oxide combined with other transition metals like MCO ( $\text{Mn}_{1.5}\text{Co}_{1.5}\text{O}_4$ ) have been used [4]. The spinel coatings reduced the oxygen diffusion inward and thereby limited the scale growth under the coatings. Froitzheim and Svensson combined a cerium coating with a cobalt coating to reduce Cr evaporation [5].

To address this need, we developed protective coatings for BOP components. Coatings of refractory ceramics such as yttria-stabilized zirconia (YSZ) and aluminum oxide ( $\text{Al}_2\text{O}_3$ ) in the form of a low-cost modified sol-gel formulation can be applied by commercially viable processes such as dip coating or conventional spraying.

The coating not only serves as a thermal barrier but also prevents Cr evaporation. YSZ coatings can be synthesized by using various techniques like electrochemical deposition (EVD) [6], plasma spray, radio frequency (RF) sputtering [7], spray pyrolysis [8], atomic layer deposition (ALD) [9], and sol-gel. A sol-gel dip coating technique was used for coating the 430SS (stainless steel) to form an oxide film. The dip coating is a low-cost coating technique and attractive alternative for large-scale manufacturing applications.

The dipping approach holds promise in specific applications:

- (i) Coating small tubes in which solution precursor plasma spray coating is difficult/problematic.
- (ii) Where ALD coating is prohibitive for large BOP components.
- (iii) A flash fire technique for larger conduit tubes can be applied by either dipping or conventionally spraying followed by infrared (IR) lamp heating inside the tube, for low-cost application.
- (iv) Solution precursor plasma spray coats one side of the substrate at a time, so surface oxidation may occur on the opposite side during the initial coating. Dipping can coat both sides simultaneously.

The barrier coating would isolate the BOP component surface from the hot humid gases within the SOFC facility and eliminate or minimize the Cr species evolution at operating temperatures of 700–900°C that can poison SOFC cathodes and degrade electrochemical performance. The engineering goal was to achieve improved stability for >40,000 hours, with an ultimate 88,000-hour or 10-year life goal. Key R&D for advanced energy systems for future coal-based power plants includes developments in protective coatings for SOFC BOP components. SOFC materials must ensure safe, reliable, and continuous operation for 10 years in harsh operating conditions (high temperatures and aggressive cell environments) to fully harness this clean energy source.

## 2. Materials and Methods

**2.1. Materials.** Zirconium (Zr) *n*-propoxide, yttrium (Y)-organics, alpha terpineol, ethylene glycol monobutyl ether acetate (BCA), ethyl acetone, diacetone alcohol, ethylcellulose (EC), lactic acid, acetylacetone, and polyethylene glycol (PEG) were procured from commercial vendors. Test samples and metallic substrates consisting of 430SS 1-inch × 1-inch and 4-inch × 4-inch plaques and 1-inch diameter tubes were similarly procured from commercial vendors. The fabricated samples were exposed to the desired atmospheres in an L & L furnace at ~800°C for 10 minutes and cooled to ambient for characterization. An IR heating

lamp (Clamp Light Portable Adjustable Pivot Metal Corded Plug-In BK-77937 E225894, with a General Electric 250R40/1 250 W 120 V R40 Med Base Clear Reflector Infrared Heat Lamp) was used to dry the samples. We used a commercial lens dipping holder (BPI Lens Holder II #16150 from Brain Power Inc., Miami, FL) designed to enable coating of the entire substrate in one dip.

**2.2. Fabrication Methods.** We formulated zirconia-yttria organic sol-gels with various chemical characteristics for dip coating adjusting the carrier solvent concentrations. In fabricating the formulation, the order of addition was critical to success. Initially, the EC was incorporated into a solvent mix of alpha terpineol and BCA. A Zr source is incorporated into a mixture of solvents. Acetylacetone was used to stabilize the zirconium *n*-propoxide, and over a short period of time, it is reported to produce Zr diketonate [10]. This enabled the zirconium material to be readily mixed with water and diacetone alcohol. Viscosity modifiers were added to achieve the appropriate rheological behavior thereby avoiding paint or ink spreading and promoting good surface leveling. This formulation and method were modified over the course of this study; the final process flow method is shown in Figure 1.

By varying the three parameters known to control solvation, the formation of stable nanoparticle sols and precipitates, the performance was optimized. In particular, nanoparticles can be formed in a stable formulation that will subsequently reduce stress during both drying and firing cycles.

From the literature, we know different precursor materials give rise to contrasted nanostructures, based on particle and agglomerate sizes. Xerogels, aerogels, and precipitates can be made by a sol-gel process in the Zr *n*-propoxide-acetylacetone-water-*n*-propanol system. Clear homogeneous sols are made by using a proper amount of acetylacetone and water. The primary control variable for not only producing clear homogeneous sols but also producing sols with some intrinsic nanoparticles in a sol-sol-gel composition is the complexation ratio *R* as shown in the following equation:

$$R = \frac{[\text{acetylacetone}]}{[\text{Zr}]}, \quad (1)$$

where *R* is the main parameter controlling the size of zirconium dioxide ( $\text{ZrO}_2$ ) primary particles. When *R* = 0, precipitates exist. The specific fractal structure of a gel largely determines whether the material becomes a xerogel, aerogel, or precipitate on conventional drying. In all cases, the initial primary units (from the literature) are ~2 nm. So, optimizing *R* allowed us to formulate a sol-gel with intrinsic particles that act as an in situ filler to avoid cracking during firing. In addition to *R* (the complexation ratio), *W* (the hydrolysis ratio) and *C* (the final metal concentration) also contribute to the stability of the sol-gel, especially with nanoparticles that will later act as stress relief agents during firing [11]. We optimized the performance using statistical design of experiments (SDEs) based on these parameters.

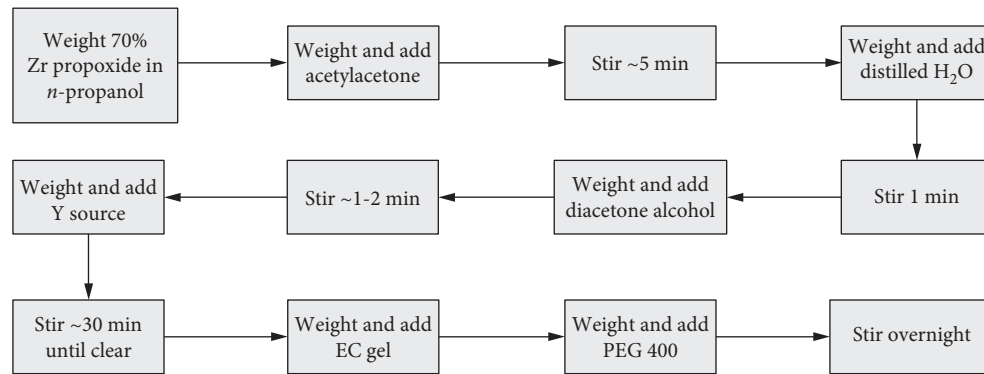


FIGURE 1: Flowchart for fabricating YSZ paint in the laboratory.

We conducted several statistically designed experiments to optimize the rheology of the YSZ and the  $\text{Al}_2\text{O}_3$  paint for dipping and stability. Stability optimization was targeted to eliminate phase separation in the form of both cloudy multiphase fluids and actual precipitation, which was macroscopically identifiable to the naked eye.

Implicit in the optimization is the generalized Landau–Levich equation used to describe a dip coating process. If shear withdrawal speed rates keep the system Newtonian (slow, 2.4 in/min to 24 in/min—we ultimately used 4 in/min), then the coating thickness is described by the following Landau–Levich equation as noted in [12–15]:

$$h = 0.945\alpha \times \text{capillary length} \times \text{capillary number} \quad (2)$$

$$= \frac{0.945(\eta v)^{2/3}}{[\gamma(1/6)(\rho g)1/2]^{1/3}}$$

where  $h$  = coating thickness,  $\alpha$  = thickening factor,  $\eta$  = viscosity,  $v$  = vertical speed,  $\gamma$  = liquid-vapor surface tension,  $\rho$  = density, and  $g$  = gravity. (The thickness factor accounts for the interaction between the surface tension and the concentration and is approximated.) So, the coating thickness depends upon control variables: viscosity, surface tension, concentration, and density.

**2.3. Test Methods.** The sol particle sizes were measured by dynamic light scattering (DLS) (University California, Irvine; Biochemistry Dept.; Irvine, CA). A fineness of grind (FOG) gauge (Gardco Fineness of Grind Gauge Model PD-250) was used to determine if there were large particulates, agglomerates, polymer ensembles, or extrinsic particulate impurities in the paint. Viscosity was characterized for various paints during the project. We used a Brookfield DV II+ Pro-LV plate and cone viscometer, although at higher shear rates the Weissenberg effect was a limitation.

The substrate camber was measured using a custom-built manual camber sorter (Figure 2). A gap was produced between the top and bottom plates using shims of known thickness. The gap was then checked using a feeler gauge.

FIGURE 2: Camber sorter. A substrate is slid down the bottom plate through the gap to the end of the two metal plates. The smallest gap distance a substrate passes through is  $D$  (Equation (3)).

This measure gap was used for camber measurements. The substrate camber is defined by the following equation:

$$C = \frac{(D - T)}{L}, \quad (3)$$

where the distance setting is  $D$ , nominal substrate thickness  $T$ , camber value is  $C$ , and substrate length is  $L$ .

The samples were dip coated using the custom dip coater shown in Figure 3. Continuity of the coating was checked by the Scotch tape test (ASTM D3359-97), optical microscopy, and scanning electron microscopy (SEM) imaging.

The primary tests for the coating qualification included thickness measurements using a FilMetrics F20 Thin Film Measurement System and a Hitachi S4500 SEM (Photo-Metrics Inc.), elemental analysis by energy dispersive X-ray spectroscopy (EDS), thermal cycling stability at 800°C, and Cr evaporation during exposure to humid air (3%  $\text{H}_2\text{O}$ ) at 800°C/500 h.

**2.3.1. Thermal Cycling at 800°C.** Thermal cycling was performed by exposing the samples to five (5) cycles at 800°C for 10 h followed by removal of the samples from the furnace. The cooling rate was 20°C/min to 600°C and then ambient cooled. This was meant to generate an initial indication of



FIGURE 3: Custom dip coater. It consists of a ring stand, ring stand clip for the samples, a CNC motor Sherline Direct 6559 machine 1-axis slide, 13" table, stepper motor and mount, CNC linear controller held by the ring stand and in a vertical position, and a glass container for the liquid.

thermal expansion and contraction data. Planar SEM micrographs were taken of the surface before and after thermal cycling.

**2.3.2. Thermal Soak at 800°C for 100 h.** The samples were isothermally aged at 800°C for 100 h in air to look for development of oxide layer growth, spalling, and weight gain. Planar SEM images were taken.

**2.3.3. Chromium Evaporation Tests.** SOFC cathodes are prone to poisoning and degradation arising from (a) impurities present in the incoming air (intrinsic and extrinsic impurities) and (b) interactions with the electrolyte. Intrinsic gas-phase impurities include water ( $H_2O$ ),  $CO_2$ , and other gas reactants. Extrinsic gas-phase impurities include various phases (some oxygen deficient) of chromium (II) oxide ( $CrO_x$ ), chromium oxyhydroxide ( $CrO(OH)_x$ ), and other Cr bearing volatile species. Degradation can be caused by solid-gas and solid-solid interactions, exsolution, and compound formation. BOP components and cell interconnections both contribute to Cr evaporation and poisoning of the cathode.

Cr evaporation (transpiration) testing was performed using the test unit shown in Figure 4. The atmosphere was held at 800°C for 500 h, with 3% water (room temperature, RT, humidification) at a flow rate of 300 sccm.

The relative humidity in air at a given temperature is fixed by the vapor pressure. The Cr vapors given off from the substrate surface are recognized to follow the laws of thermodynamics. The resulting theoretical behavior is shown in Figures 5 and 6. Figure 6 shows the dependence of

Cr vapor species concentration on temperature and  $H_2O$  concentration expressed as partial pressure. It can be seen that the partial pressure of the Cr species increases with temperature, as expected thermodynamically.

With respect to the Cr vapor in equilibrium with  $Cr_2O_3$ , the thermodynamic calculations show a relationship between temperature at a given percent water in air and the partial pressure of Cr plus the partial pressure of  $Cr_2O(OH)_2$ , in Figure 6. The atmosphere is assumed to be essentially ambient air, with a  $P(O_2)$  of 0.209 atm—the normal  $P(O_2)$  in air.

Figure 7 is a schematic representation of the typical two-phase boundary and three-phase boundary reactions from Cr-bearing species evaporated from BOP components that can react with an LSM oxide such as  $La_{0.7}Sr_{0.3}MnO_3$  or LSM-based cathodes.

In Figure 8, we see the various chemical reactions that can take place at an LSM cathode, due to Cr poisoning. In all the cases, the integrity of the LSM is compromised. The result is a change in the chemistry and therefore the electrochemistry of the cathode, rendering it incapable of performing its proper electrochemical function in the SOFC.

**2.3.4. Statistically Designed Experiments.** Statistically designed experiments were conducted and analysed with the assistance of Design Expert 8 software (Stat-Ease, Inc.).

### 3. Results and Discussion

We conducted several statistically designed experiments to optimize the rheology of the YSZ and the  $Al_2O_3$  paint for dipping and stability. Stability optimization was targeted to eliminate phase separation in the form of both cloudy multiphase fluids and actual precipitation, which was macroscopically identifiable to the naked eye. The most significant correlation diagram for YSZ is shown in Figure 9. Note:  $R$  = complexation ratio,  $W$  = hydrolysis ratio, and  $C$  = final metal concentration. Figure 9 shows a statistically significant relationship among separation,  $R$  and  $W$ . When  $C$  is high, a strong dependence exists between  $R$  and  $W$ . Only when  $C$  is high do we find that when  $R$  is low, there is phase separation. When  $W$  is high, separation increases even more. This correlation has a 93% confidence limit. In looking at the implications, we found phase separation is eliminated if the acetylacetone concentration is high and the water concentration is low.

For alumina formulations, there was severe precipitation. A statistically designed experiment was conducted and the degree of precipitation was indexed from 0 (no precipitation) to 1 (severe precipitation). Precipitation only occurs if the ethyl acetone is high. The concentrations for acetone, aluminum acetylacetonate, and the other constituents had no significant effect on precipitation. The ethyl acetone concentration was lowered to eliminate precipitation.

A FOG gauge was used to determine if there were large particulates, agglomerates, polymer ensembles, or extrinsic particulate impurities in the paint. The results are reported as

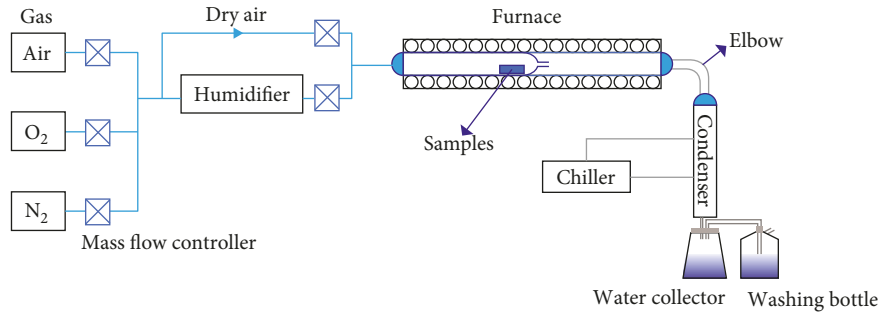


FIGURE 4: Schematic of Cr evaporation test units at University of Connecticut.

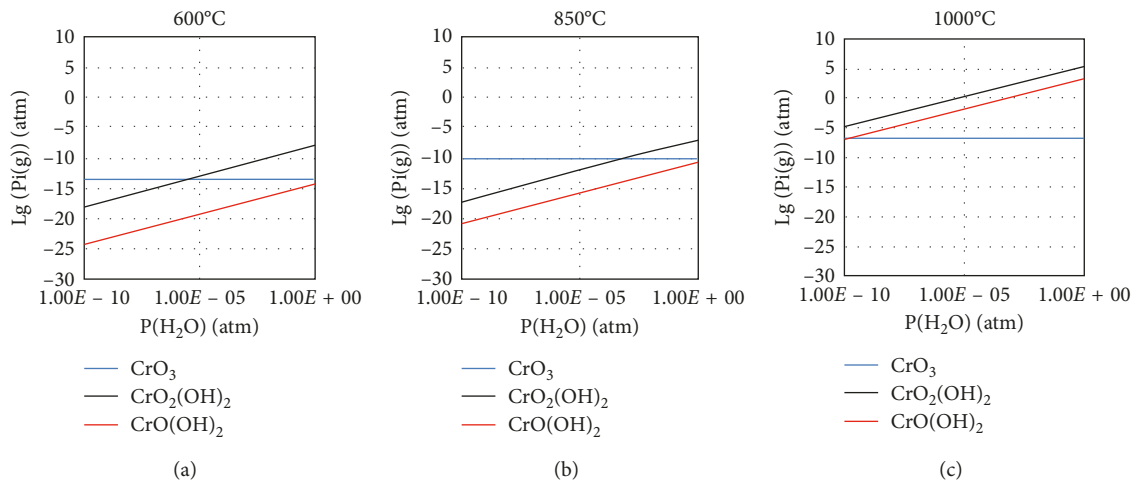


FIGURE 5: Partial pressures of chromium vapor species varying with the partial pressure of  $H_2O$  under different temperatures. (a)  $600^\circ C$ ; (b)  $850^\circ C$ ; (c)  $1000^\circ C$ . Wherein,  $P(O_2) = 0.209$  atm (partial pressure of oxygen in air).

1st scratch, 4th scratch, and 50% size, with all measurements at  $<2 \mu m$ . The detection limit is  $2 \mu m$ . Larger ( $>2 \mu m$ ) agglomerates were not observed.

DLS intensity was analysed to determine the particle-size distribution function. For the YSZ formulations, the DLS average particle size was in the range of 1,000–2,000 nm (Table 1). This may be due to, to some extent, an effective particle size for YSZ plus associated layers of EC and water of hydration. The DLS data are consistent with the FOG measurements indicating the particle size for all the YSZ powders is  $<2 \mu m$ . The alumina-based sample shows an initial low DLS particle size of  $\sim 4$  nm. However, over time the 102615-SZ-3087-A11 formulation showed precipitation, and this is borne out by the FOG gauge measurements of  $\sim 40 \mu m$ .

Viscosity of dipping paints or inks were measured. At higher shear rates, the Weissenberg effect was a limitation. After the issue of precipitation was eliminated, the viscosity was reasonably stable, compared with the measurement error. The viscosity was varied over a wide range to develop an appropriate rheology for dipping, which balances a high YSZ or  $Al_2O_3$  content with a low viscosity for good dipping, 2.21–270.7 (at 1.5 RPM) to 115–416.8 (at 9 RPM).

The thicknesses of sample coatings were measured using a Filmetrics Thin-Film Measurement System. The values ranged from 0.20 to  $1.66 \mu m$ . There is significant variation in

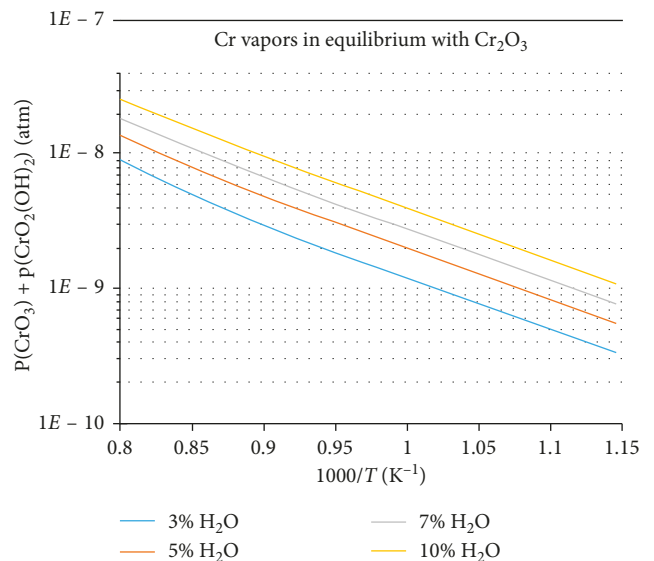


FIGURE 6: Partial pressures of chromium vapor species varying with temperature for different partial pressures of  $H_2O$ . Wherein,  $P(O_2) = 0.209$  atm (partial pressure of oxygen in air).

thickness, in part dependent upon the uniformity of the substrate. The valleys are filled, and due to surface energy, the asperities are lightly covered. Considering that

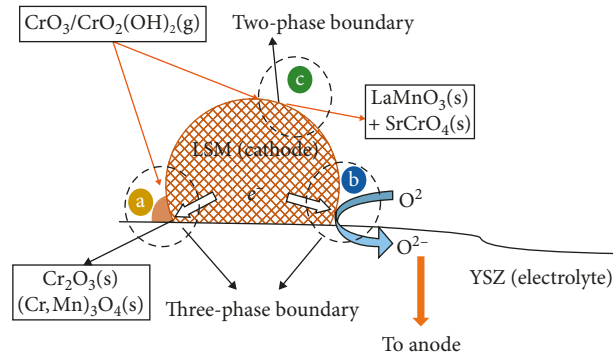


FIGURE 7: A schematic representation of the general types of Cr poisoning reactions that may take place: two-phase boundary reactions and three-phase boundary reactions.

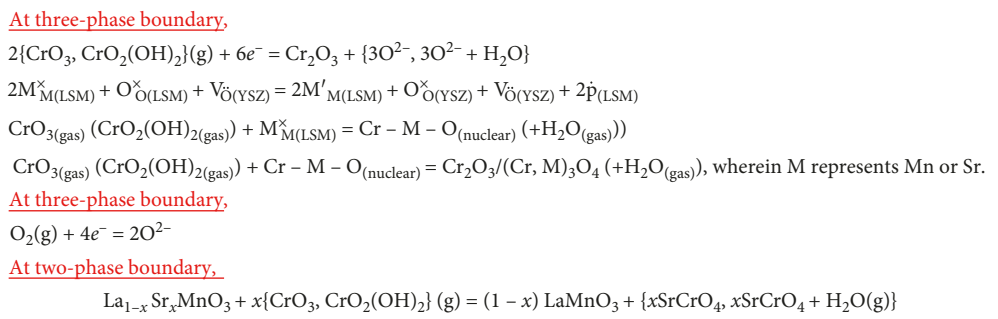


FIGURE 8: Typical reactions that may take place at an LSM cathode from Cr poisoning.

Filmetrics' interferometric technique depended upon having a flat and parallel film structure with respect to the non-transparent substrate, the values are only approximate.

Ten 430SS substrates that had been laser cut into 1-inch  $\times$  1-inch substrates were measured for the camber. The average camber was  $0.000 \pm 0.002$  mm/mm (in/in). The maximum camber was 0.003 mm/mm (in/in). This camber can be interpreted as representative of general shape variation. In BOP components, the shape nonuniformity in, for example, ductwork, is expected to be considerably worse.

**3.1. Coating 1 in.  $\times$  1 in.  $\times$  0.025 in. 430SS Substrates.** One issue was the need to dip samples twice for complete coverage. We found that, in dipping the entire flat edge of the substrate, there was substantial paint buildup that led to cracking during drying and firing. This effect was minimized by dipping down to one corner (the diamond orientation in Figure 3). To demonstrate a holder design that would enable the coating of the entire substrate in one dip, we obtained a commercial lens dipping holder. To minimize the effects of dust on the uniformity of the coating, a laminar flow booth was used. The dip speed, dip dwell time, and dip depth were regulated by a computer numerical control (CNC) linear controller. The sample with the holder was then transferred to a drying area, where the wet substrate was dried at a fixed distance from an IR heating lamp. After this drying step,

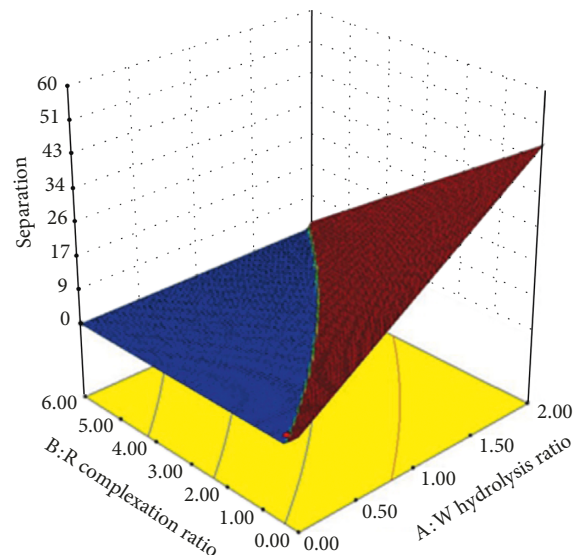


FIGURE 9: Graph showing the correlations between  $R$ ,  $W$ , and separation for high final metal concentration. When  $C$  is high, a strong dependence exists between  $R$  and  $W$ . Only when  $C$  is high do we find that when  $R$  is low, there is phase separation, and it increases further when  $W$  is high (93% confidence limit). We found phase separation is eliminated if acetylacetone is in high concentration and the water concentration is low.

TABLE 1: The average particle size found for several formulation paints from DLS.

Paint formulation	Material	$d$ (nm)	Std. dev. (nm)
090315-SZ-3087-15-NA1	YSZ	1058	345.8
091015-SZ-3087-15-NA1	YSZ	1219	480
101215-SZ-32087-15-NA1	YSZ	1915	1209
102615-SZ-3087-All	Al <sub>2</sub> O <sub>3</sub>	25.62	4.1

some formulations were still not fully cured. These were placed in a small Petri dish with a loose lid to dry. Substrate films were dry before firing.

**3.2. Firing Profile through YSZ Nucleation and Growth.** In the literature, nucleation and growth has been reported for the 8 mol% Y-doped ZrO<sub>2</sub> system, with the nucleation range lower than the crystal growth temperature range. The nucleation and growth curves for sol-gel-derived YSZ show nucleation in the range of 380 to  $\geq 400^\circ\text{C}$  [16] and crystal growth in the range of  $400^\circ\text{C}$ – $500^\circ\text{C}$  for sol-gel-derived YSZ depositions [17]. However, in this work, we found our paint has a typical suspended particle size of  $\sim 1\ \mu\text{m}$  for YSZ and  $\sim 25\ \text{nm}$  for Al<sub>2</sub>O<sub>3</sub>. Nucleation and growth was checked by optical and SEM imaging. Little or no such growth was found, with the only identifiable particles being  $\sim 200\ \text{nm}$ .

After exposure to  $800^\circ\text{C}$  for 10 minutes, the surface showed no evidence of the presence of grain formation. However, after 100 h at  $800^\circ\text{C}$ , substantial sintering neck growth occurred with grain sizes of  $\sim 200\ \text{nm}$ , demonstrating some densification but no grain growth. The grain size is uniform, with no exaggerated grain growth, although some grain growth would be expected for long firing times,  $> 100\ \text{h}$ .

**3.3. Thermal Cycling and Heat Soak Results.** The samples were exposed to  $650^\circ\text{C}$  for 10 minutes followed by  $800^\circ\text{C}$  for 10 minutes to minimize the surface coating spallation during firing as well as removal of organic constituents. The samples are described in Table 2.

The YSZ coating withstands thermal cycling and isothermal aging to 100 h at  $800^\circ\text{C}$ . Al<sub>2</sub>O<sub>3</sub> coating sample quality however varied. Sample B137 (Table 2) does not withstand thermal cycling. Sample B108 does withstand thermal cycling; however, the quality is not good.

**3.4. Thermal Cycling at  $800^\circ\text{C}$ .** Thermal cycling was performed by exposing the samples for five (5) cycles at  $800^\circ\text{C}$  for 10 h followed by removal of the samples from the furnace. The cooling rate was  $20^\circ\text{C}/\text{min}$  to  $600^\circ\text{C}$  and then ambient cooled. This was meant to generate an initial indication of thermal expansion and contraction data. Two samples (YSZ-B131 and Al<sub>2</sub>O<sub>3</sub>-B137) were tested. Planar SEM micrographs were taken of the surface before and after thermal cycling (Figures 10 and 11).

Above observations clearly indicate that YSZ is superior to Al<sub>2</sub>O<sub>3</sub>, in that Al<sub>2</sub>O<sub>3</sub> spalled off during the thermal cycling, particularly during handling between cycles. The spalling was sufficient to render the weight gain measurements invalid since some materials pulled off and actually decreased the overall weight of the sample.

**Evaluation of Multilayer Coated Samples.** Characterization of the coating was performed to identify mechanisms needed for uniform coverage. We made multiple coatings on 430SS 1-inch  $\times$  1-inch substrates. Each layer was dipped, dried, and fired for 10 minutes at  $800^\circ\text{C}$ . Cr evaporation can be decreased by relatively thin film coatings, which can be classified into two main groups perovskite structure and spinel structure coatings.

From the EDS, with Mn, Cr, and O, with  $\text{Cr} < \text{Mn}$ , the stoichiometry from Figures 12(a) and 12(b) appears to be  $\text{Mn}_x\text{Cr}_3-x\text{O}_4$ , with  $x \sim 2$ . Fe is from the substrate. The tentative conclusion is that we are looking at the 430SS substrate from below the surface and crystals of spinel  $\text{Mn}_x\text{Cr}_3-x\text{O}_4$ , with  $x \sim 2$ .

The effect of using a multiple-layer coating process on the morphology and adhesion of YSZ to 430SS post-annealing treatment was evaluated. Figures 13(a)–13(d) show the surface morphology of the YSZ coating using SEM microscopy. The intensity of the cracks decreased with the increase of the deposition cycles of the YSZ coating. Fewer cracks were observed at the edge of the sample when compared to the center, in contrast to what had been seen with 1-2 layer coatings. However, the edge area also shows fewer cracks, as the number of layers increases.

Figures 13(e)–13(j) show that the addition of the YSZ nanopowder increases the intensity of the cracks for fewer deposition layers (2 and 3), while the intensity of the cracks decreases as the number of layers increases. The YSZ film covered the 430SS substrate. Microcracks observed on all the samples could affect the protection ability of the YSZ film. The round shape of the grain edges observed in Figures 13(g)–13(j) may have formed due to the volatilization of the grain boundary phases.

The energy dispersive X-ray analysis of all the samples showed the presence of Y and Zr in the stoichiometric ratio, within experimental error. The intensity of the cracks on the YSZ coatings decreased with the increase of the deposition cycles both with and without the addition of the nanopowder. The Cr evaporation decreased by 51% for a single YSZ layer coating (B146) sample, with no nanopowder YSZ added. It was then compared with an uncoated sample (B151)—both were tested on a 1 in.  $\times$  1 in. 430SS substrate.

**3.5. Thermal Soak at  $800^\circ\text{C}$  for 100 h.** The samples were isothermally aged at  $800^\circ\text{C}$  for 100 h in air to look for development of oxide layer growth, spalling, and weight gain. Planar SEM images are shown for YSZ-B123 and Al<sub>2</sub>O<sub>3</sub>-B127 (Figure 14). The content of Zr and Y at the B123 surface is much higher than the B132 sample seen in Figure 15. From EDS, the Cr content at the B123 surface is also less than the

TABLE 2: Characteristics of the substrates used in coating and testing.

Sample	Substrate	Surface	Sol-gel material	Firing
B123	430 1 in. × 1 in. laser cut	2000 grit	111715-3087-SZ-YSZ-Scaleup	650°C-10 min + 800°C-10 min
B131	430 1 in. × 1 in. laser cut	2000 grit	112015-SZ-3087-YSZ-Scaleup-4	650°C-10 min + 800°C-10 min
B132	430 1 in. × 1 in. laser cut	2000 grit	112015-SZ-3087-YSZ-Scaleup-4	650°C-10 min + 800°C-10 min
B127	430 1 in. × 1 in. laser cut	2000 grit	111315-SZ-3087-Al7-4-Scaleup	650°C-10 min + 800°C-10 min
B107	430 1 in. × 1 in. laser cut	2000 grit	111315-SZ-3087-Al7-4-Scaleup	650°C-10 min + 800°C-10 min
B108	430 1 in. × 1 in. laser cut	2000 grit	111315-SZ-3087-Al7-4-Scaleup	650°C-10 min + 800°C-10 min
B137	430 1 in. × 1 in. laser cut	2000 grit	111315-SZ-3087-Al7-4-Scaleup	650°C-10 min + 800°C-10 min
B138	430 1 in. × 1 in. laser cut	2000 grit	111315-SZ-3087-Al7-4-Scaleup	650°C-10 min + 800°C-10 min
B140	430 1 in. × 1 in. laser cut	Bare	None	None
B141	430 1 in. × 1 in. laser cut	Bare	None	None

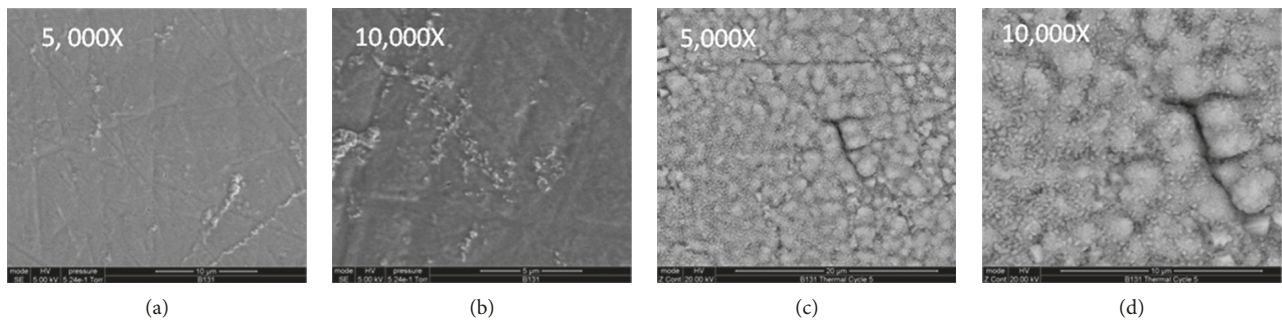


FIGURE 10: Sample YSZ-B131 before and after thermal cycling. (a) Before thermal cycling, shown at 5,000X. (b) Before thermal cycling, shown at 10,000X. (c) After thermal cycling, shown at 5,000X. (d) After thermal cycling, shown at 10,000X. The nonthermally cycled sample EDX shows only iron (Fe), Y, Zr, and oxygen (O).

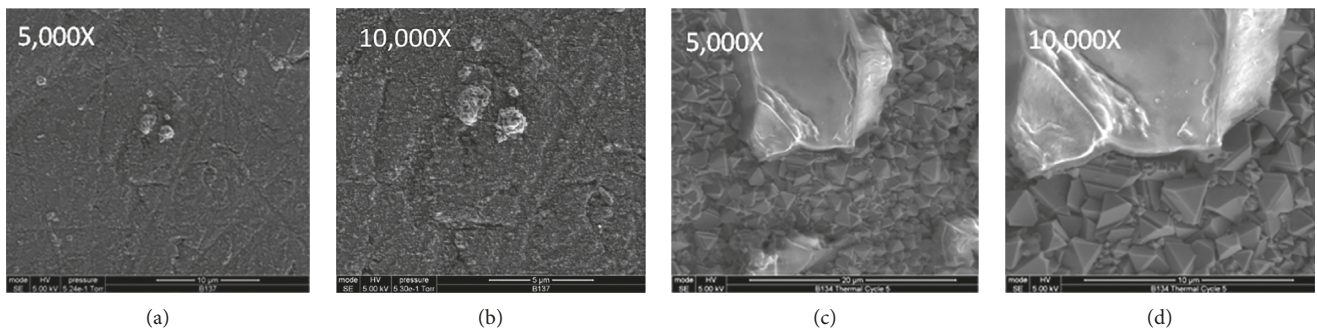


FIGURE 11: Sample Al<sub>2</sub>O<sub>3</sub>-B137 before and after thermal cycling. (a) Before thermal cycling, shown at 5,000X. (b) Before thermal cycling, shown at 10,000X. (c) After thermal cycling, shown at 5,000X. (d) After thermal cycling, shown at 10,000X. The nonthermally cycled sample EDX shows only iron (Fe), aluminum (Al), silica (Si), carbon (C), and oxygen (O). Fe, Si, and C are in the substrate. No Cr or Ni are detected.

B132 sample. The observation is possibly related to the coating thickness and the spatial resolution for EDS analysis. B127 surface morphology is similar to the uncoated sample. However, aluminum (Al) is detected at the surface. It is likely that Al may have reacted with the substrate oxide layer.

EDS was performed on various areas of the YSZ-B123 sample. From the micrograph (Figure 14), the coating appears to be  $\sim 1 \mu\text{m}$  thick. Crystals are seen underneath the coating. It appears that the crystals are probably manganese (Mn)-Cr-iron (Fe)-oxygen (O) spinels, such as  $\text{MnFe}_2\text{O}_4$

and  $\text{Mn}_x\text{Cr}_3-x\text{O}_4$ . From an EDS, showing Mn, Cr, and O, with  $\text{Cr} < \text{Mn}$ , the surface appears to be  $\text{Mn}_x\text{Cr}_3-x\text{O}_4$ , with  $x \sim 2$ . Fe is from the substrate. The tentative conclusion is that we are looking at the 430SS substrate from below the surface and crystals of spinel  $\text{Mn}_x\text{Cr}_3-x\text{O}_4$ , with  $x \sim 2$ .

The SEM image of the cross section of the thermally soaked B-123 (YSZ) sample is shown in Figure 16. Four distinct phases are observed as marked. The EDS spot analyses (Table 3) reveal the composition of these phases. The dark colored phases (spot 1) are enriched of chromium, manganese, and iron while the content of these elements

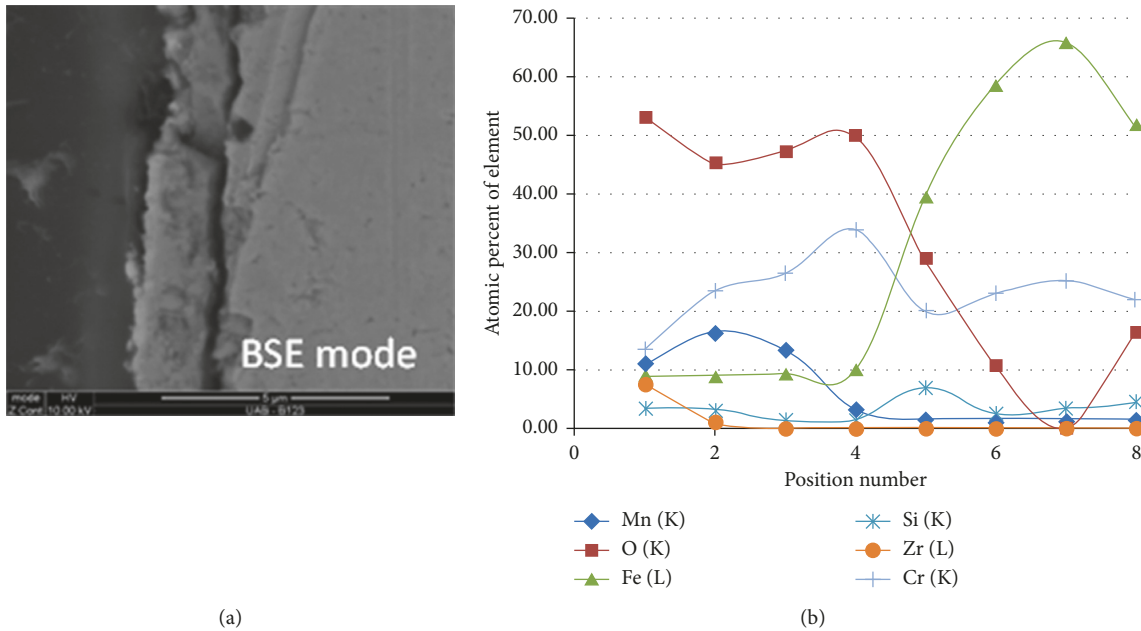


FIGURE 12: YSZ-B123: EDX analyses were run fairly evenly spaced in a line from 1 through 8 for the thermally soaked sample.

decreases for the brighter phases. The oxygen content increases for the brighter phases and is highest for the spots labeled 4. The zirconium content is higher for the spots 1 and 4. Several interferences are made from the observation. Firstly, oxygen and zirconium diffuse inward and other elements diffuse outward. Secondly, silicon diffuses throughout the coating. Thirdly, the oxide layers consist of  $\text{Cr}_2\text{O}_3$ , Mn-Cr-O, and Mn-Fe-O spinels. The content of these phases varies for different layers (spots). Zirconium likely dissolves in these phases in the form of solid-solution.

The EDX line scan is shown in Figure 17. The line scan is consistent with the EDX spot analysis and supports the aforementioned interpretation. However, the cause for the decrease in oxygen content in the spot 1 (Figure 16) region is unknown.

The EDX elemental maps of the B-123 sample are shown in Figure 18. Juxtaposing the elemental images supports the above interpretations.

The SEM image of the cross section of the thermally soaked B-127 ( $\text{Al}_2\text{O}_3$ ) sample is shown in Figure 19. Three distinct layers are observed as marked. The EDX spot analyses (Table 4) reveal that the thin dark layer near the interface is enriched with silicon, chromium, and iron. Layer 2 is enriched of chromium while layer 3 is enriched of chromium and manganese. Only a very small quantity of aluminum is detected in layer 3. The layer 1 is likely to be  $\text{SiO}_2$ , which acts a protective oxide layer. Layer 2 is likely to be  $\text{Cr}_2\text{O}_3$ , and layer 3 is Cr-Mn-O spinel.  $\text{Al}_2\text{O}_3$  coating may have spalled of the oxidized sample. Therefore, it is not detected.

The line scan in Figure 20 shows the presence of silicon, as seen by the hump in the Si profile followed by humps in chromium and oxygen profile. Lastly, chromium content

decreases and manganese increases as observed by the hump in the manganese profile. These observations support the EDS spot analysis and suggest the presence of the  $\text{SiO}_2$  layer followed by  $\text{Cr}_2\text{O}_3$  and Mn-Cr-O spinel, which is complemented by the EDX elemental maps in Figure 21.

**3.6. Cr Evaporation Tests.** SOFC cathodes are prone to poisoning and degradation arising from (1) impurities present in the incoming air (intrinsic and extrinsic impurities) and (2) interactions with the electrolyte. Intrinsic gas-phase impurities include  $\text{H}_2\text{O}$ ,  $\text{CO}_2$ , and other gas reactants. Extrinsic gas-phase impurities include  $\text{CrO}_x$ ,  $\text{CrO}(\text{OH})_x$ , and other Cr bearing volatile species. Degradation can be caused by solid-gas and solid-solid interactions, exsolution, and compound formation.

A Cr evaporation test was run on two, 1-inch  $\times$  1-inch  $\times$  0.020-inch, 430SS substrates, one uncoated and one coated. The two samples were run separately. The images of the Cr-bearing evaporated material can be seen visually on the interior of the exit condenser in Figure 22, especially when comparing the two 500 h results. The 500 h image clearly shows the uncoated sample has much more of the yellow-brown condensate than the coated sample. The collaborators at the University of Connecticut extracted the Cr bearing material from the condenser and ran inductively coupled plasma atomic emission spectroscopy (ICP). As can be seen, there is significantly more Cr deposited from the uncoated sample (Figure 22).

The Cr bearing material that was found in the condenser tube at the end of the Cr tester was washed out after the completion of each Cr evaporation test. The resultant solution was taken, and ICP analysis was used to measure the

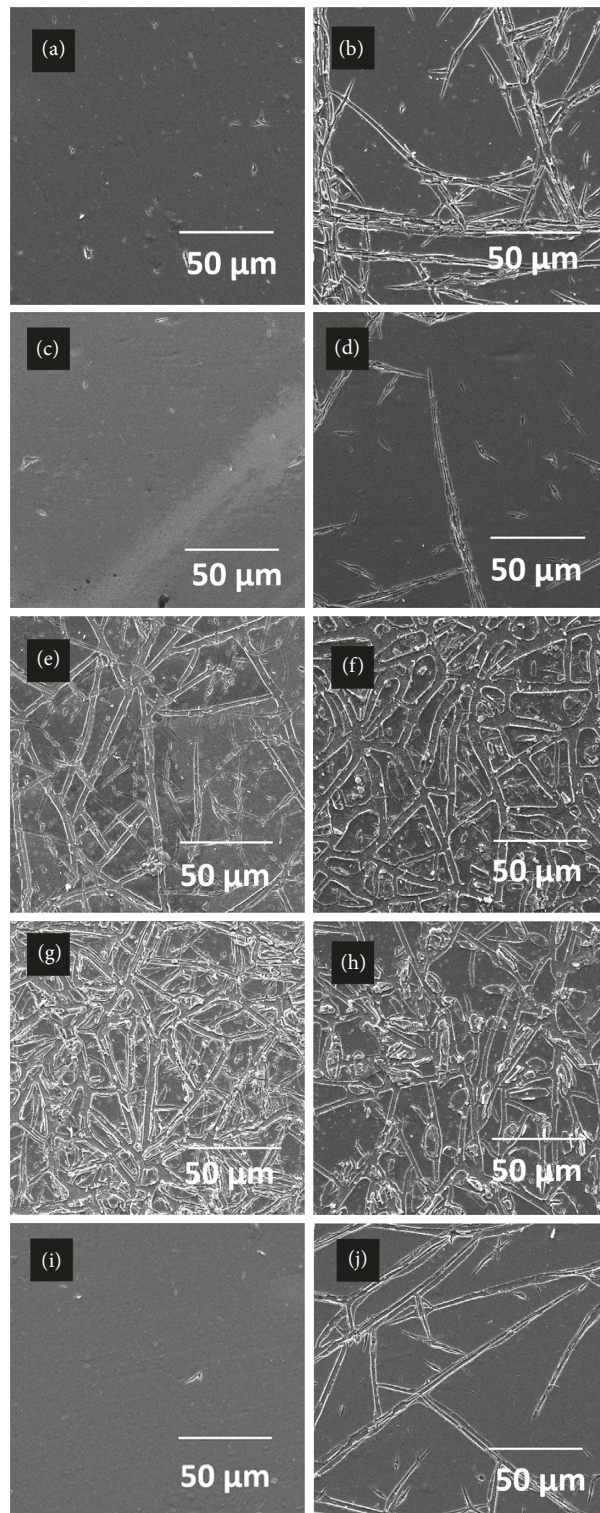


FIGURE 13: YSZ-coated 430 stainless steel. (a) Edge; (b) center of the sample after four (4) deposition cycles using dip coating. (c) Edge; (d) center of the sample after five (5) deposition cycles using dip coating. (e) Edge; (f) center of the sample after two (2) deposition cycles using dip coating. (g) Edge; (h) center of the sample after three (3) deposition cycles using dip coating. (i) Edge; (j) center of the sample after four (4) deposition cycles using dip coating.

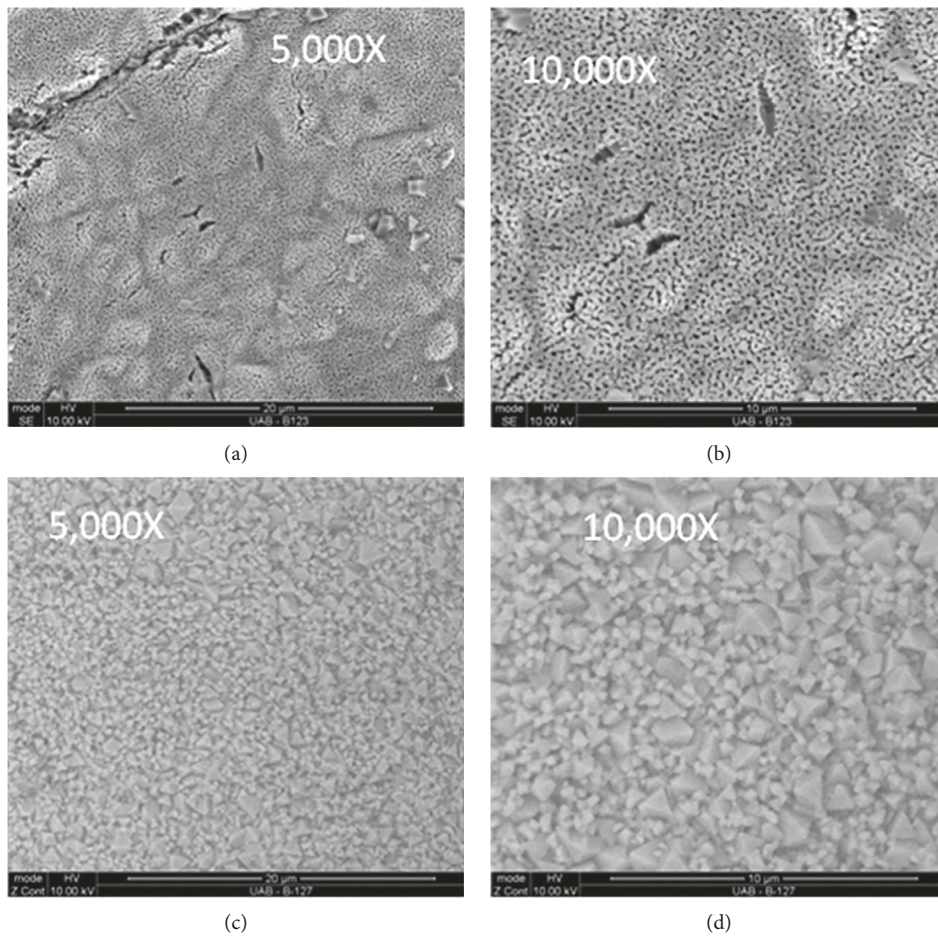


FIGURE 14: Thermal soak samples. (a) Sample YSZ-B123 at 5,000X. (b) Sample YSZ-B123 at 10,000X. (c) Sample Al<sub>2</sub>O<sub>3</sub>-B127 at 5,000X. (d) Sample Al<sub>2</sub>O<sub>3</sub>-B127 at 10,000X.

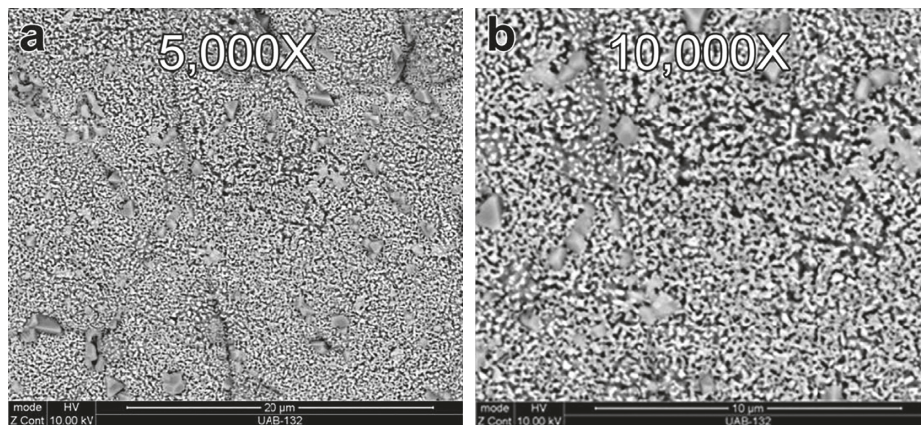


FIGURE 15: Thermal soak samples: YSZ-B132 (a) at 5,000X and (b) at 10,000X.

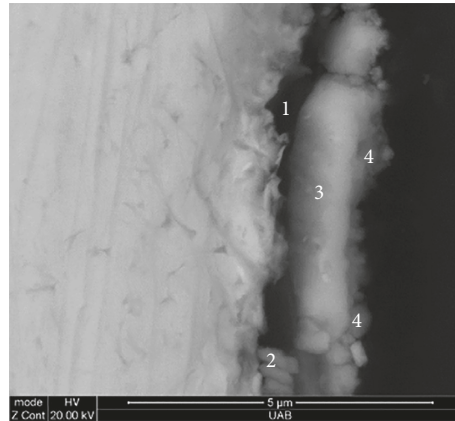


FIGURE 16: SEM image of cross section of the B-123 (YSZ) sample.

TABLE 3: The elemental analysis (EDS spot) for the different phases (marked) in Figure 16 (atomic percent).

Elements	1	2	3	4
O	$43.9 \pm 4.5$	$57.5 \pm 3.2$	$63.8 \pm 3.7$	$69.2 \pm 2.0$
Si	$2.3 \pm 0.1$	$1.9 \pm 0.3$	$2.2 \pm 0.9$	$2.6 \pm 1.1$
Cr	$20.5 \pm 2.4$	$19.1 \pm 1.1$	$17.7 \pm 1.1$	$9.7 \pm 1.4$
Mn	$9.7 \pm 1.0$	$6.0 \pm 0.6$	$4.9 \pm 0.3$	$5.2 \pm 1.2$
Fe	$18.3 \pm 0.7$	$13.6 \pm 0.9$	$9.7 \pm 2.2$	$9.5 \pm 1.0$
Y	$0.5 \pm 0.1$	$0.2 \pm 0.1$	$0.2 \pm 0.0$	$0.3 \pm 0.0$
Zr	$4.8 \pm 0.5$	$1.6 \pm 0.4$	$1.4 \pm 0.3$	$3.5 \pm 1.3$

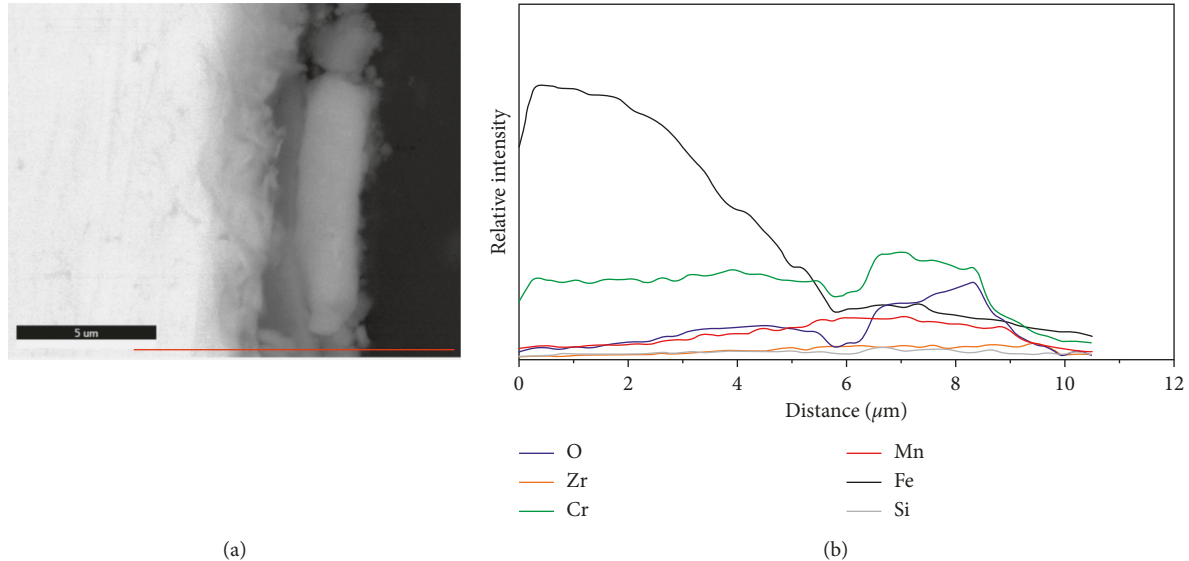


FIGURE 17: Line scan analysis of the cross section of the B-123 (YSZ) sample. (a) EDS spot analysis. (b) Line scan.

amount of Cr for the bare and the coated substrates. The data are shown in Table 5. The coating decreased the Cr evaporation by  $\sim 51\%$ . This demonstrates that even with some areas not fully covered, there was a reduction in the Cr evaporation due to the coating.

The SEM images of substrates are shown in Figure 23, at different magnifications for 500 h in the  $800^\circ\text{C}$  Cr evaporation test. The uncoated 430SS 1-inch  $\times$  1-inch  $\times$  0.020-

inch shows the growth per the thermal growth oxide (TGO) scale. The coated specimen shows the surface with some protective coating, although there are open, uncoated areas that can be seen in some cases for the coated specimen.

We focused on developing and evaluating a coating to reduce or eliminate Cr evaporation for BOP SOFC components. Coating performance was improved and cost minimized by using flash firing at  $800^\circ\text{C}$  for 10 minutes.

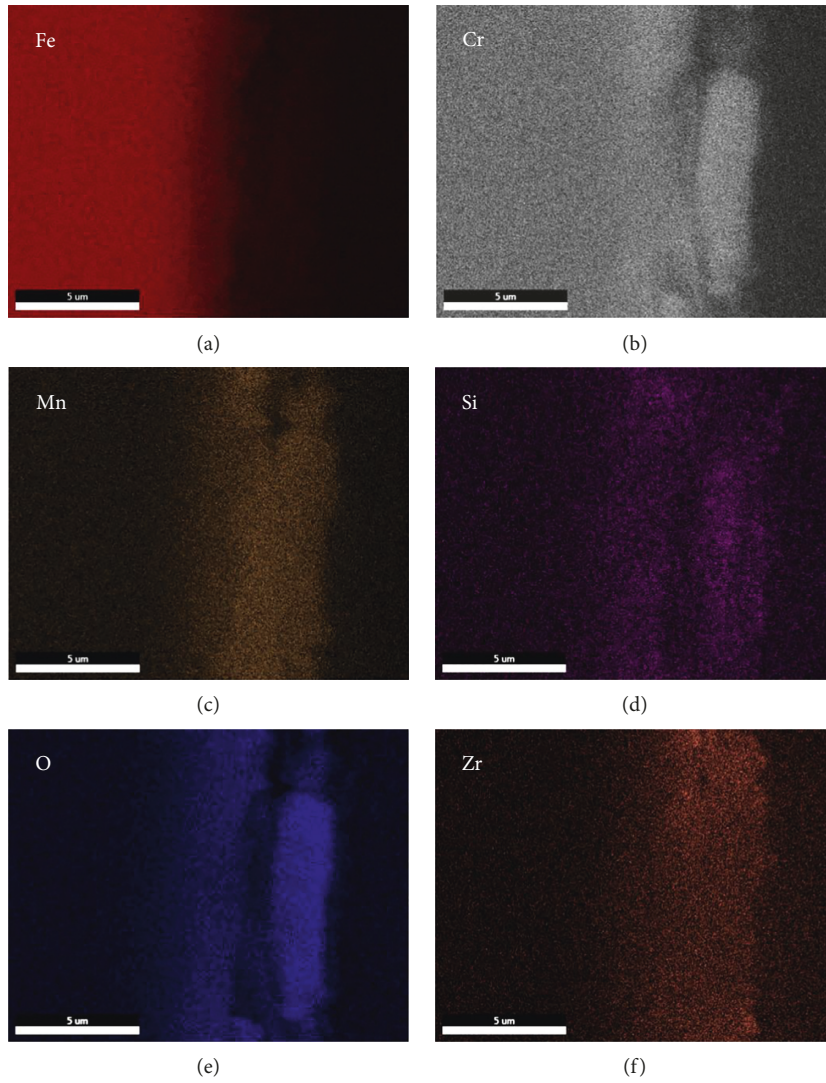


FIGURE 18: Elemental maps of the cross section of the B-123 (YSZ) sample.

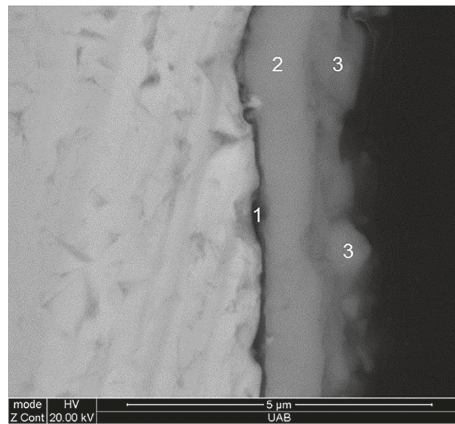


FIGURE 19: SEM image of cross section of the B-127 ( $\text{Al}_2\text{O}_3$ ) sample.

We used a model GS1714 Furnace with Honeywell UDC3300 program control and DC2500 over temperature protection. The samples were vertically mounted in slits

cut into a silica ceramic foam monolith  $\sim 4$  in.  $\times$   $\sim 4$  in.  $\times$   $\sim 2$  in. holder. The holder with the sample was introduced into the hot furnace chamber, held at target test temperature of

TABLE 4: The elemental analysis (EDS spot) for the different phases (marked) in Figure 19 (atomic percent).

Elements	1	2	3
O	33.5 ± 10.1	55.6 ± 0.3	58.6 ± 1.1
Al	0.1 ± 0.2	0.7 ± 0.3	1.7 ± 0.5
Si	4.8 ± 2.5	1.4 ± 0.2	2.2 ± 0.6
Cr	31.3 ± 7.8	28.9 ± 0.2	23.6 ± 1.4
Mn	2.3 ± 0.3	2.3 ± 0.2	9.2 ± 1.0
Fe	27.7 ± 2.6	11.0 ± 0.6	4.7 ± 0.5

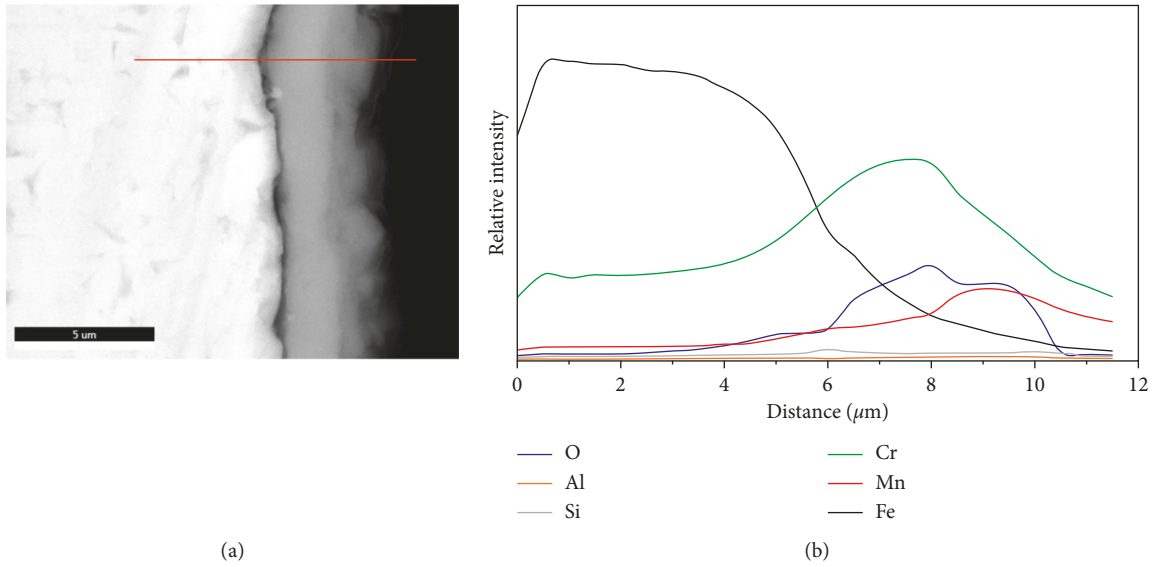


FIGURE 20: Line scan analysis of the cross section of the B-127 (YSZ) sample.

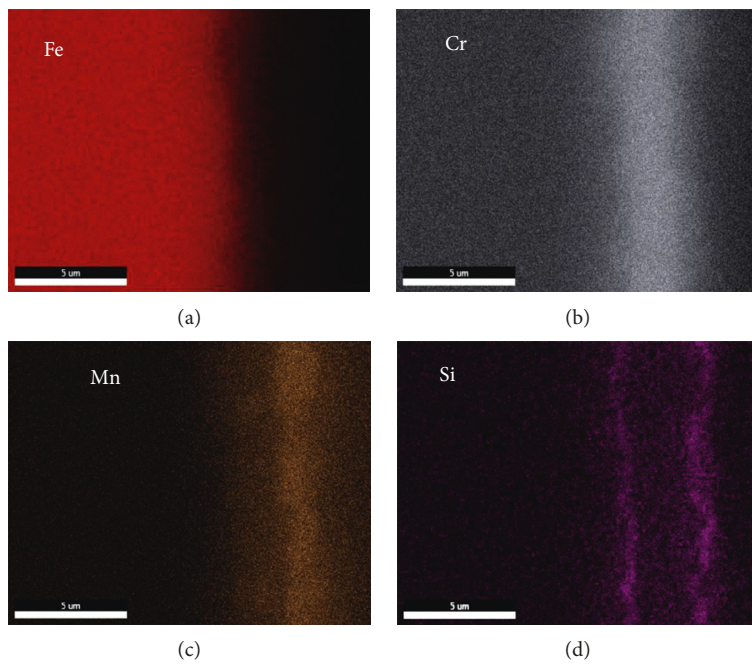


FIGURE 21: Continued.

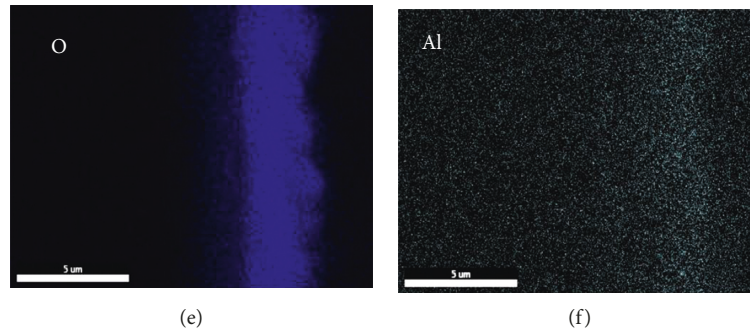


FIGURE 21: Elemental maps of the cross section of the B-123 (YSZ) sample.

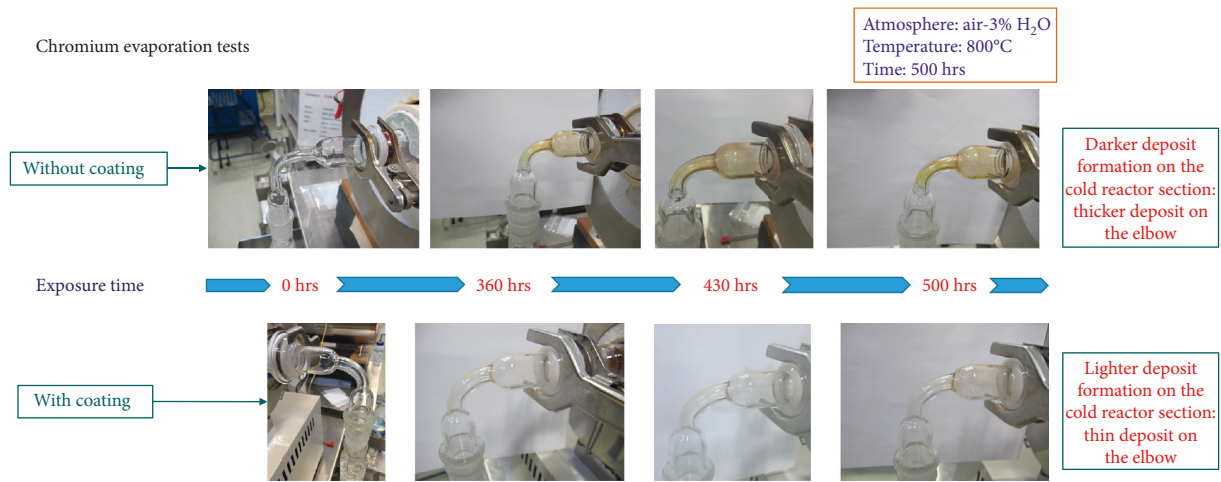
FIGURE 22: Cr evaporation test images of uncoated and YSZ-coated 430SS 1-inch  $\times$  1-inch  $\times$  0.020-inch samples showing condensate at various intervals for 500 h at 800°C.

TABLE 5: Concentration of Cr found in the materials deposited in the condensers from the Cr evaporation testing at 800°C for 500 h.

Samples	Total Cr mass (g) evaporated during 500 hrs	Surface area of samples ( $m^2$ )	Evaporation rate of $Cr_2O_3$ ( $kg/m^2s$ )	Partial pressure of Cr vapors in 300 sccm air flux (atm)
B-146 (SS430 coated with YSZ)	$1.89 E - 04$	$1.30 E - 03$	$2.36 E - 10$	$3.56041 E - 08$
B-151 (bare SS430)	$3.87 E - 04$	$1.32 E - 03$	$4.76 E - 10$	$7.27762 E - 08$

800°C and after 10 minutes, the holder with samples was removed and allowed to cool at ambient. After cooling, samples were removed and stored for testing.

Additional coating improvement and potential cost reduction were achieved through improved dipping and handling technology. We identified areas for fine-tuning and more rigorous testing. We had demonstrated the following:

- (i) Dipping formulations showed better overall performance for YSZ than  $Al_2O_3$ . The clear, nonphase separated modified YSZ sol-gel formulation was easily scaled up from 10 g to  $\sim$ 250 g.
- (ii) Initial firing at 800°C resulted in macroscopically continuous coatings, with good adhesion.
- (iii) 430SS substrate coatings, after heat thermal soak at 800°C for 100 h, are adherent,  $\sim$ 50% porous on

a nanoscale, and nanograined YSZ. They have a thickness of  $\sim$ 100 nm– $1 \mu m$  and a pore size of  $\sim$ 200 nm.

- (iv) Spalling in the form of small flakes could be found under certain process conditions, both before and after firing. This was minimized by optimizing process conditions. We switched to flash firing (as previously described) and redesigned the dip holder design. We also optimized composition.
- (v) Although initial flash 800°C firing (as previously described) can result in continuous coatings with good adhesion, subsequent thermal soak at 800°C after 100 h resulted in a nanoporous fine grain ( $\sim$ 200 nm) structure and what appears to be

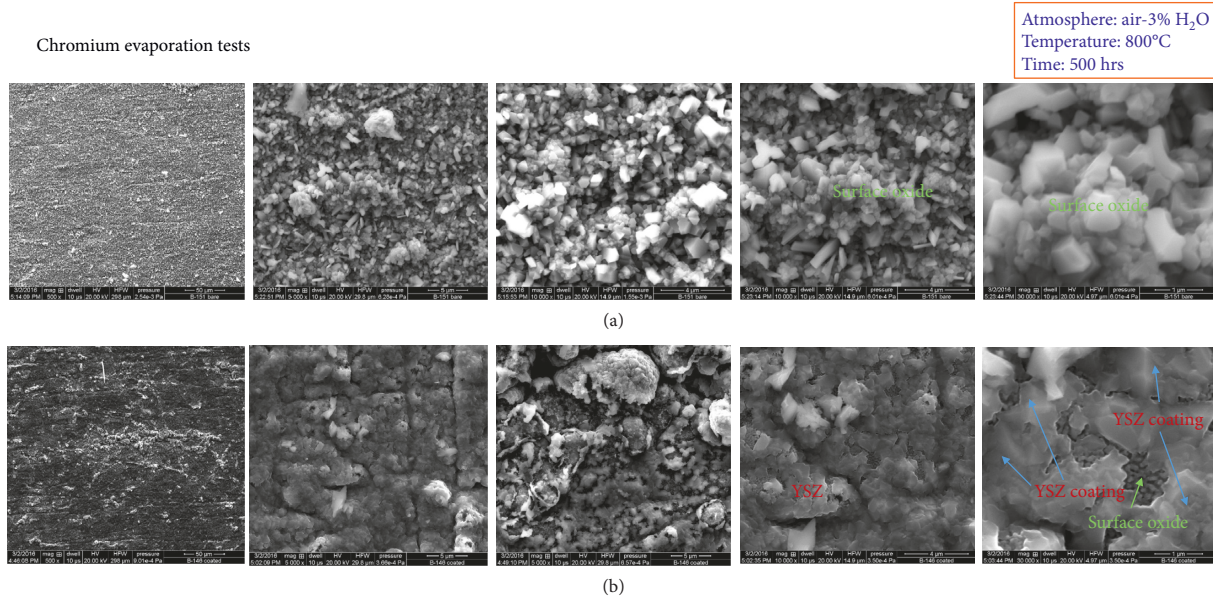


FIGURE 23: Cr evaporation test: SEM images of (a) uncoated and (b) YSZ-coated 430SS substrates (1-inch  $\times$  1-inch  $\times$  0.020-inch) shown at various magnifications following 500 h at 800°C in air/3% H<sub>2</sub>O atmosphere.

a surface reaction layer (possible spinel formation) under the YSZ layer.

- (vi) The transformation of an apparently dense layer to a nanoporous layer can be explained in several different ways that could be clarified in future work:
  - (a) Resolution of SEM for nanopores
  - (b) Free volume within the surface state and vitreous state is eliminated by thermal treatment
  - (c) Material leaving the YSZ coating, as appears to occur for Y
  - (d) A combination of the above
- (vii) Literature reports are consistent in recognizing the following:
  - (a) Porous structures result from 800°C firings. Diffusion only becomes an effective transport mechanism above 800°C, where time improves densification.
  - (b) Coatings containing YSZ are adherent and homogeneous, with cracks that can be reduced by optimizing the alkoxide sol content.
- (viii) Some of these issues can be addressed by sequential dip-fire cycles. As the number of layers is increased, the thickness and surface roughness both increase.
- (ix) The thickness of the thermally grown oxide (apparently a Mn-Cr-O spinel) is thinner with a YSZ coating ( $\sim 1.5 \mu\text{m}$ ) than for uncoated samples ( $\sim 3.5 \mu\text{m}$ ).
- (x) Even a relatively thin (100 nm– $1 \mu\text{m}$ ) YSZ coating reduced the Cr evolution by  $\sim 51\%$  (500 h at 800°C)

compared with an uncoated sample of the same substrate material (430SS). This suggests that with increase in coating thickness and a denser surface coverage, significant reduction to complete elimination of Cr evaporation can be achieved with the YSZ coatings.

- (xi) The intensity of the cracks on the YSZ coatings decreased with the increase of the deposition cycles both with and without the addition of the nanopowder.

These initial results have provided insight about where future efforts should be focused.

#### 4. Conclusions

We demonstrated feasibility through dip coating and firing samples of 430SS substrates in various sizes and shapes. Samples were tested by thermal cycling/soak and Cr-species evaporation. A  $\sim 51\%$  reduction in Cr-species evaporation was measured for the YSZ-coated substrate compared to an uncoated substrate after 500 h at 800°C. Metallographic cross sections show that the intermetallic layer over the 430SS surface for the BOPSeal-coated surface is about 1/3 the thickness for the non-BOPSeal-coated surface. Results also indicate that the intensity of the cracks on the YSZ coatings decreased with increasing layers, with and without the addition of the nanopowder. We will pursue increasing the number of layers with and without additions of YSZ nanopowder to increase the coating coverage protecting the stainless steel surface. The result is envisioned to substantially decrease/eliminate Cr evaporation from BOP components for SOFCs. Optimized coatings would support protective barrier layers for (1) SOFC

BOP components, (2) bioreactors, and (3) seals in YSZ electrolytes for manifolds used in space applications.

## Data Availability

The data used to support the findings of this study are available from the corresponding author upon request.

## Conflicts of Interest

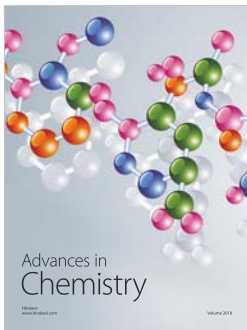
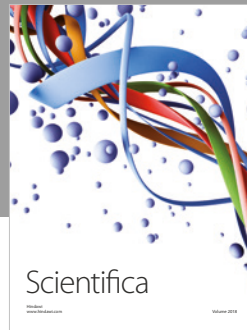
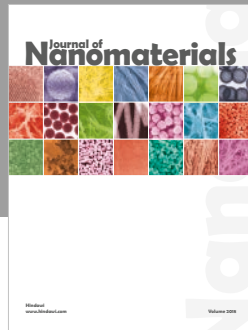
There are no conflicts of interest. The sol-gel formulations discussed in this paper are proprietary.

## Acknowledgments

Mr. Steven R. Markovich, Program Manager, U.S. Department of Energy, National Energy Technology Laboratory, Pittsburgh, is acknowledged for technical discussions during the course of the program. This material is based on the work supported by the U.S. Department of Energy (Office of Science and Office of Fossil Energy (Award Number: DE-SC0013879)).

## References

- [1] M. Stanislowski, J. Froitzheim, L. Niewolak et al., "Reduction of chromium vaporization from SOFC interconnectors by highly effective coatings," *Journal of Power Sources*, vol. 164, no. 2, pp. 578–589, 2007.
- [2] H. Kurokawa, C. P. Jacobson, L. C. DeJonghe, and S. J. Visco, "Chromium vaporization of bare and of coated iron–chromium alloys at 1073 K," *Solid State Ionics*, vol. 178, no. 3–4, pp. 287–296, 2007.
- [3] S. Chevalier, C. Valot, G. Bonnet, J. C. Colson, and J. P. Larpin, "The reactive element effect on thermally grown chromia scale residual stress," *Materials Science and Engineering: A*, vol. 343, no. 1–2, pp. 257–264, 2003.
- [4] Z. Yang, G.-G. Xia, C.-M. Wang et al., "Investigation of iron–chromium–niobium–titanium ferritic stainless steel for solid oxide fuel cell interconnect applications," *Journal of Power Sources*, vol. 183, no. 2, pp. 660–667, 2008.
- [5] J. Froitzheim and J.-E. Svensson, "Multifunctional nano-coatings for SOFC interconnects," *ECS Transactions*, vol. 35, no. 1, pp. 2503–2508, 2011.
- [6] U. B. Pal and S. C. Singhal, "Electrochemical vapor deposition of yttria-stabilized zirconia films," *Journal of The Electrochemical Society*, vol. 137, no. 9, pp. 2937–2941, 1990.
- [7] F. Smeacetto, M. Salvo, L. C. Ajitdoss et al., "Yttria-stabilized zirconia thin film electrolyte produced by RF sputtering for solid oxide fuel cell applications," *Materials Letters*, vol. 64, no. 22, pp. 2450–2453, 2010.
- [8] D. Perednis, O. Wilhelm, S. E. Pratsinis, and L. J. Gauckler, "Morphology and deposition of thin yttria stabilized zirconia films using spray pyrolysis," *Thin Solid Films*, vol. 474, no. 1–2, pp. 84–95, 2005.
- [9] J. H. Shim, C. C. Chao, H. Huang, and F. B. Prinz, "Atomic layer deposition of yttria-stabilized zirconia for solid oxide fuel cells," *Chemistry of Materials*, vol. 19, no. 15, pp. 3850–3854, 2007.
- [10] Y. Xie, *Solution-based synthesis and processing of nanocrystalline zirconium diborides-based composites*, Ph.D. thesis, Georgia Institute of Technology, Atlanta, GA, USA, 2008.
- [11] G. Zhang, Z. Rasheva, J. Karger-Kocsis, and T. Burkhart, "Synergetic role of nanoparticles and micro-scale short carbon fibers on the mechanical profiles of epoxy resin," *Express Polymer Letters*, vol. 5, no. 10, pp. 859–872, 2011.
- [12] C. J. Brinker, "Dip coating," in *Chemical Solution Deposition of Functional Oxide Thin Films*, Schneller, Ed., p. 237, Springer-Verla, Wien, Europe, 2013, <https://www.unm.edu/~solgel/PublicationsPDF/2013/BrinkerDipCoating2013.pdf>.
- [13] H. Schmidt and M. Mennig, "Wet coating technologies for glass," in *The Sol-Gel Gateway*, Institut für Neue Materialien, Saarbrücken, Europe, 2000, <http://www.solgel.com/articles/nov00/mennig.htm>.
- [14] I. Strawbridge and P. F. James, "The factors affecting the thickness of sol-gel silica coatings prepared by dipping," *Journal of Non-Crystalline Solids*, vol. 86, no. 3, pp. 381–393, 1986.
- [15] H. C. Mayer and R. Krechetnikov, "Landau-Levich flow visualization: revealing the flow topology responsible for the film thickening phenomena," *Physics of Fluids*, vol. 24, no. 5, article 052103, 2012.
- [16] T. Barnardo, *Time resolved anomalous small angle X-ray scattering of the sol-gel process*, Ph.D. thesis, Aberystwyth University, Wales, UK, 2010.
- [17] S. Heiroth, R. Frison, J. L. M. Rupp et al., "Crystallization and grain growth characteristics of yttria-stabilized thin films grown by pulsed laser deposition," *Solid State Ionics*, vol. 191, no. 1, pp. 12–23, 2011.



**Hindawi**  
Submit your manuscripts at  
[www.hindawi.com](http://www.hindawi.com)

